Journal of Environmental Science International
35(10); 963~980; October 2026

pISSN: 1225-4517 eISSN: 2287-3503
https://doi.org/10.5322/JESI.2026.35.10.963

ORIGINAL ARTICLE

Genetically Engineered M13 Bacteriophage Displaying Adipose Homing Peptide and 4E Sequence for Targeted Anti-Adipogenic Therapy

Sun Young Park[1)], Jin-Woo Oh[1,2)], Geuntae Park[1,2,3)*]

[1)]*Institute of Nanobio Convergence, Pusan National University, Busan 46241, Korea*
[2)]*School of Advanced Convergence Future Energy major, Pusan National University, Busan 46241, Korea*
[3)]*Convergence Department, Graduate School, Pusan National University, Busan 46241, Korea*

Abstract

Obesity is a major metabolic disorder characterized by excessive adipogenesis and lipid accumulation, and there remains a pressing need for effective and safe therapeutic strategies. Filamentous M13 bacteriophage provides a highly programmable nanoplatform that can be engineered to display bioactive peptides on its coat proteins, enabling targeted biological functions. This study presents a novel nanotherapeutic approach utilizing genetically engineered M13 phage as a biocompatible macromolecular platform for targeted obesity treatment. M13 phage was genetically modified to display adipose homing peptide (AHP, CKGGRAKDC) on the minor coat protein pIII for tissue-specific targeting and 4E peptide sequence (EEEE) on the major coat protein pVIII for anti-adipogenic activity. Comprehensive structural characterization using cryo-transmission electron microscopy and dynamic light scattering confirmed successful peptide incorporation while preserving native phage architecture. The engineered variants demonstrated distinct physicochemical properties, with M13 4E-AHP exhibiting enhanced negative surface charge and increased hydrodynamic diameter compared to wild-type controls. Functional validation of AHP targeting specificity was demonstrated through prohibitin receptor analysis, showing marked increased expression in differentiated adipocytes following M13 AHP treatment. In vitro studies using 3T3-L1 preadipocytes demonstrate that M13 4E and M13 4E-AHP variants operate through coordinated multi-level intervention in adipogenic differentiation. The M13 4E and M13 4E-AHP simultaneously preserve preadipocyte morphology, dramatically reduce lipid synthesis and storage, modulate glycerol metabolism, and suppress expression of master adipogenic transcription factors and lipogenic enzymes. The biological macromolecule platform exhibited excellent biocompatibility with no observed adverse effects across all tested conditions. These findings establish M13 4E-AHP phage as a promising biological macromolecule-based therapeutic system for obesity treatment, offering superior safety profiles compared to synthetic nanoparticles and providing a strong foundation for further therapeutic development.

Key words : M13phage engineering, Biological macromolecules, Targeted drug delivery, Anti-adipogenic peptides, Nanomedicine

1. Introduction

Obesity represents a multifactorial chronic disease characterized by excessive fat accumulation that fundamentally disrupts normal physiological processes throughout the human body. This complex metabolic disorder results from intricate interactions between physiological factors including genetics, behavior, and psychology, combined with environmental influences such as sociocultural elements (Jin et al., 2023; Kong et al., 2025). The pathophysiology

Received 28 September, 2026; **Revised** 13 October, 2026;
Accepted 14 October, 2026
***Corresponding author** : Geuntae Park, Department of Nanofusion Technology, Graduate School, Pusan National University, Busan 46241, Korea
Phone : +82-51-510-3740
E-mail : gtpark@pusan.ac.kr

© The Korean Environmental Sciences Society. All rights reserved.
This is an Open-Access article distributed under the terms of the Creative Commons Attribution Non-Commercial License (http://creativecommons.org/licenses/by-nc/3.0) which permits unrestricted non-commercial use, distribution, and reproduction in any medium, provided the original work is properly cited.

of obesity centers on energy imbalance between consumption and expenditure, particularly affecting genetically susceptible individuals, leading to characteristic fat accumulation in white adipose tissue. The clinical significance of obesity extends far beyond aesthetic concerns, as it substantially increases the risk of numerous comorbidities associated with high morbidity and mortality rates. Altered glucose metabolism secondary to obesity has been directly linked to hypertension, type 2 diabetes mellitus, and cardiovascular complications. Additionally, individuals with BMI ≥ 25 demonstrate increased susceptibility to gallbladder disease, gallstone formation, and osteoarthritis compared to their lean counterparts (Gao et al., 2015; Rupert and Kolonin, 2022; Li et al., 2022). Furthermore, accumulating evidence has established strong associations between obesity and multiple cancer types, underscoring the systemic impact of this metabolic disorder (Antwi et al., 2012; Ataey et al., 2020; Pati et al., 2023). While dietary modifications and lifestyle interventions demonstrate independent efficacy in obesity management, sustaining these behavioral changes remains challenging, as evidenced by frequent weight regain patterns observed in clinical practice (Mahamat-Saleh et al., 2024; Xiao et al., 2024). Consequently, several FDA-approved anti-obesity pharmacotherapies have entered the market, with numerous additional compounds currently in development pipelines. However, existing anti-obesity medications primarily function through appetite suppression or satiety enhancement rather than addressing the underlying pathophysiology of obesity. Moreover, many of these therapeutic agents have been associated with serious cardiovascular or psychiatric adverse effects, highlighting the critical need for alternative treatment strategies (Gao et al., 2021; Xian et al., 2023).

The emerging paradigm of targeted therapy represents a revolutionary approach to overcoming the limitations of conventional treatments by delivering therapeutic agents directly to disease sites, thereby maximizing drug efficacy while minimizing systemic side effects. In the context of obesity, targeting adipose tissue—the primary site of pathological fat accumulation—offers a direct and potentially powerful intervention strategy. This approach leverages the concept of molecular "address tags" that can selectively deliver therapeutic agents to specific tissue types (Salameh et al., 2016; Daquinag et al., 2021). Adipose homing peptides (AHP) have emerged as promising molecular targeting tools for obesity treatment. The AHP sequence CKGGRAKDC has been specifically identified for its ability to bind selectively to prohibitin, a protein highly expressed on the surface of endothelial cells within white adipose tissue. This specific receptor–ligand interaction enables selective delivery of therapeutic agents to adipose tissue while potentially reducing off-target effects in healthy organs (Salameh et al., 2016; Daquinag et al., 2021; Safari et al., 2022).

M13 phage represents a versatile and biocompatible nanoscale platform with extensive therapeutic potential across multiple biomedical applications. As a filamentous virus measuring approximately 880 nm in length and 6.6 nm in diameter, M13 possesses unique structural characteristics that make it particularly suitable for bioengineering applications. The M13 phage surface consists of approximately 2,700 copies of the major coat protein pVIII, which comprises about 98% of the viral surface area, providing extensive opportunities for genetic modification and peptide display (Jin and Lee, 2018; Chang et al., 2023; Fadaie et al., 2023; Yang and Chen, 2024; de Medeiros Dantas et al., 2025). The remarkable advantage of M13 phage lies in its capacity for genetic manipulation without

compromising structural integrity or functional viability. Amino acid sequences can be successfully inserted into the M13 phage structure through chemical or genetic modification approaches, enabling the incorporation of cell signaling peptides that can induce desired cellular functions (Gu et al., 2022; Wang et al., 2023; Nazeri et al., 2025). Importantly, no harmful effects on mammalian cells have been reported, establishing M13 as a safe therapeutic platform. The self-assembling nature of M13 phage creates attractive nanostructural components capable of expressing various peptides on their surface, facilitating mass replication and assembly into nanostructures suitable for tissue regeneration applications. These unique properties position M13 phage as an ideal nanoscale platform for stem cell engineering and targeted therapeutic applications (Safari et al., 2022; Rahimi et al., 2023; Kim et al., 2024).

The present study introduces a novel dual modification strategy for M13 phage engineering to create a multifunctional therapeutic agent for obesity treatment. The first modification involves genetic fusion of the AHP sequence (CKGGRAKDC) to the minor coat protein pIII, enabling specific targeting of white adipose tissue through prohibitin receptor binding. This targeting mechanism ensures selective delivery of the therapeutic agent to the primary sites of pathological fat accumulation. The second critical modification involves the substitution of the N-terminal region of the major coat protein pVIII with a 4E sequence. This pVIII protein engineering represents a novel approach designed specifically to confer intrinsic anti-obesity properties to the M13 phage platform. The 4E mutation involves replacing specific amino acid residues with glutamic acid (E), thereby altering the surface charge distribution and modulating the physicochemical properties of the pVIII protein. Previous research on M13 pVIII protein mutations, including 4E variants, has demonstrated that such modifications can significantly influence the hydrophobicity and ionic interactions of the M13 phage surface, potentially enhancing functional capabilities while maintaining structural stability and host infectivity (Jin and Lee, 2018; Wang et al., 2023; Kim et al., 2024). The 4E mutation has been identified as a representative variant from pVIII mutation libraries, with charge alterations contributing to M13 phage surface modification and binding affinity regulation. This investigation aims to evaluate the therapeutic potential of specifically engineered M13 phage for obesity treatment through comprehensive in vitro cellular studies and in vivo animal experimentation. We hypothesize that the combination of AHP-mediated adipose tissue targeting via pIII protein modification and the anti-obesity functionality conferred by pVIII protein 4E substitution will create an effective and safe therapeutic nanoplatform.

The study employs 3T3-L1 preadipocyte and mature adipocyte culture models to assess the dual functionality of our engineered M13 phage system. Through systematic evaluation of tissue targeting specificity, adipogenic differentiation, and lipid accumulation, we aim to demonstrate the therapeutic potential of this novel targeted nanomedicine approach.

2. Materials and Methods

2.1. Genetic engineering of M13 4E-AHP

To engineer M13 phage displaying peptide motifs on all copies of the major (pVIII) and minor (pIII) coat proteins, inverse polymerase chain reaction (PCR) cloning methodology was employed following the site-directed mutagenesis protocol (New England Biolabs, Ipswich, MA, USA). M13 phage presenting 4E peptides (EEEE) at the N-terminus of all pVIII copies and adipose

homing peptide (AHP, CKGGRAKDC) at the N-terminus of all pIII copies were constructed using inverse PCR amplification. The amplified plasmids were verified by DNA sequencing performed at Cosmogenetech Inc. (Seoul, South Korea) to confirm successful insertion of the target sequences.

2.2. M13 4E-AHP purification and preparation

M13 phage were isolated by combining elements of the Phage-on-Tap procedure with polyethylene glycol (PEG) precipitation. Mid-log phase bacterial cultures grown in 25 mL of LB medium were infected with phage stocks and incubated at 37°C with shaking for 16 h. After centrifugation at 7,000 × g for 30 min, cell-free supernatants were treated with DNase I (1 μg/mL; Roche Diagnostics) at 37°C for 2 h, followed by sterile filtration through 0.22 μm membranes. Phages were precipitated overnight at 4°C in 0.5 M NaCl and 8% PEG 8000 (Millipore Sigma). Viral pellets were collected by centrifugation (7,000 × g, 30 min), resuspended in SM buffer (200 mM NaCl, 10 mM $MgSO_4$, 50 mM Tris-HCl, pH 7.5), and subjected to a second round of PEG precipitation. The resulting phage pellets were again resuspended in SM buffer and treated with 1-octanol at 4°C for 2 h to reduce endotoxin levels. Preparations were then dialyzed against SM buffer for 48 h using 50 kDa Spectra Por Float-A-Lyzer G2 devices (Cole-Parmer) and titrated by the double agar overlay assay.

2.3. Endotoxin assessment of M13 4E-AHP

To verify endotoxin content in M13 phage preparations, Limulus amoebocyte lysate (LAL) assays were performed using the Pierce Chromogenic Endotoxin Quantitation Kit (Thermo Fisher Scientific). Purified M13 phage preparations were diluted in SM buffer to working concentrations (1×10^7 PFU/mL) and subjected to LAL testing according to the manufacturer's protocol. Endotoxin content for each M13 phage preparation at working concentrations is presented in Table 1.

Table 1. Titers of M13 phage and endotoxin levels

Phage	Titer (PFU/ml)	Experimental endotoxin (10^7 PFU/mL/3T3L-1) (EU/mL)
M13	2.98×10^9	0.12
M13 4E	5.77×10^9	0.13
M13 AHP	2.24×10^9	0.12
M13 4E-AHP	4.87×10^9	0.14

2.4. Physicochemical characterization of M13 4E-AHP

Dynamic light scattering (DLS) measurements were performed using a Malvern Panalytical Zetasizer Nano-ZS90 sample delivery system to determine hydrodynamic diameter (Z-average), polydispersity index (PDI), zeta potential, and conductivity of the engineered M13 phage variants. M13 phage samples were diluted in SM buffer to appropriate concentrations and equilibrated at room temperature prior to analysis. All measurements were conducted in triplicate with automatic measurement positioning and duration optimization.

2.5. Structural analysis of M13 4E-AHP

Cryo-transmission electron microscopy (Cryo-TEM) imaging was performed using a Krios G4 system to assess the morphological integrity of engineered M13 phage variants. Samples were prepared according to standard cryo-TEM protocols and imaged to confirm preservation of filamentous structure following genetic modifications.

2.6. 3T3-L1 preadipocyte culture and adipogenic differentiation

Murine 3T3-L1 preadipocytes (catalog CL-173, lot 70047755) were procured from the American Type Culture Collection (Manassas, VA, USA) and maintained in Dulbecco's Modified Eagle Medium/Nutrient Mixture F-12 (DMEM/ F-12) supplemented with 10% heat-inactivated fetal bovine serum and 1% penicillin-streptomycin antibiotic solution. Cell cultures were maintained at 37°C in a humidified atmosphere containing 5% CO_2. For adipogenic differentiation induction, preadipocytes were cultured until reaching approximately 100% confluence. Following a 48-hour post-confluence period, differentiation was initiated using a commercial 3T3-L1 Differentiation Kit (BioVision, Milpitas, CA, USA). The differentiation protocol consisted of a three-phase treatment regimen: Phase I involved 72-hour exposure to complete differentiation medium containing 1 μM dexamethasone, 500 μM 3-isobutyl-1-methylxanthine (IBMX), 1.5 μg/mL insulin, and 1 μM rosiglitazone. Phase II comprised 48-hour culture in DMEM/F-12 medium supplemented with 1.5 μg/mL insulin only. Phase III involved maintenance culture with medium replacement every 48 hours until experimental endpoints. M13 phage treatments (M13, M13 4E, M13 AHP, and M13 4E-AHP) were administered as 2-hour pretreatments prior to differentiation medium exposure and maintained throughout the 9-day experimental period to evaluate anti-adipogenic efficacy.

2.7. Cell viability assessment

Cell viability was determined using the Cell Counting Kit-8 (CCK-8) colorimetric assay (Sigma-Aldrich-Merck KGaA, Burlington, MA, USA). Preadipocytes and mature adipocytes were seeded at 1×10^4 cells per well in 48-well culture plates and incubated under standard culture conditions. Following 48-hour equilibration, cells received 2-hour phage pretreatments followed by differentiation medium exposure where appropriate. Cell viability assessment was performed by adding CCK-8 reagent at a 1:100 dilution to culture wells, followed by 4-hour incubation in light-protected conditions at 37°C. Metabolic activity was quantified by measuring optical density at 450 nm using a Wallac Victor microplate reader (PerkinElmer Corporation, Norwalk, CT, USA). Results were expressed as percentage viability relative to untreated control cultures.

2.8. Lipid droplet visualization and quantification

Following 9-day differentiation culture, intracellular neutral lipid accumulation was assessed using a commercial Oil Red-O Staining Kit (BioVision, Milpitas, CA, USA). Cultured adipocytes were washed twice with sterile phosphate-buffered saline (PBS), fixed in 10% neutral buffered formalin for 30 minutes at ambient temperature, and subsequently stained with Oil Red-O working solution for 60 minutes. Microscopic visualization was performed using bright-field optics, and digital images were captured for qualitative assessment. For quantitative analysis, cell-associated Oil Red-O dye was extracted using isopropanol solvent, and lipid content was determined by spectrophotometric measurement at 490 nm wavelength. Complementary lipid droplet analysis was performed using a Nile Red Staining Kit (Abcam, Cambridge, UK). Preadipocytes were seeded at 4×10^3 cells per well in 8-well chamber slides (Thermo Fisher Scientific) and differentiated according to established protocols. Following differentiation, cells were washed with PBS, fixed in 10% formalin buffer, and incubated with Nile Red solution for 30 minutes at room temperature. Fluorescence microscopy was performed using a confocal laser scanning microscope (LSM 800, Carl Zeiss, Jena, Germany) with appropriate excitation/ emission wavelengths for Nile Red detection.

2.9. Triglyceride content analysis and glycerol secretion assessment

Cellular triglyceride accumulation was evaluated through enzymatic colorimetric methodology utilizing a commercial Triglyceride Colorimetric Assay Kit (Cayman Chemical Company, Ann Arbor, MI, USA) applied to prepared cell lysates. Simultaneously, extracellular glycerol release was monitored by analyzing culture medium supernatants through an EZ-free Glycerol Assay Kit (Dogenbio Co., Seoul, Republic of Korea). Both analytical procedures were executed following manufacturer-provided protocols with appropriate quality controls and standard curves for quantitative determination.

2.10. Gene expression profiling by reverse transcription-quantitative PCR

Total cellular RNA isolation was accomplished using the PureLink RNA Mini Kit extraction system, followed by concentration determination via NanoDrop spectrophotometric analysis (Thermo Scientific, Waltham, MA, USA). Complementary DNA synthesis was performed using high-capacity reverse transcription reagents according to standard protocols. Quantitative gene expression analysis was conducted employing SYBR Green-based real-time PCR Master Mix chemistry on a Bio-Rad Chromo4 thermal cycling platform (Applied Biosystems, Hercules, CA, USA). Amplification reactions were performed in triplicate within 96-well plate format using standardized thermal cycling conditions: initial denaturation followed by 40 cycles of 95°C denaturation (15 seconds) and 58°C annealing/extension (40 seconds). Target-specific oligonucleotide primer sequences are detailed in the accompanying primer table. Relative gene expression quantification was calculated using the comparative threshold cycle ($2^{-\Delta\Delta Ct}$) analytical method with appropriate housekeeping gene normalization controls.

2.11. Prohibitin expression analysis and functional validation

For protein-based analysis of prohibitin expression, cultured adipocytes were subjected to complete cellular lysis using mammalian cell extraction buffer (Thermo Fisher Scientific, Waltham, MA, USA) supplemented with protease inhibition cocktail (Sigma-Aldrich, St. Louis, MO, USA). Cell lysates were maintained on ice for 30 minutes with periodic agitation to ensure complete protein solubilization, followed by high-speed centrifugation at 12,000 × g for 10 minutes at 4°C to remove cellular debris. Clarified protein supernatants were collected and total protein concentrations were determined using Bradford colorimetric assay methodology (Bio-Rad Laboratories, Hercules, CA, USA). Protein samples were prepared for electrophoretic separation by thermal denaturation and loaded onto Mini-PROTEAN precast polyacrylamide gels (Bio-Rad Laboratories) for sodium dodecyl sulfate-polyacrylamide gel electrophoresis (SDS-PAGE). Following electrophoretic separation, proteins were transferred to polyvinylidene difluoride membranes (Hybond PVDF, Amersham Biosciences, Little Chalfont, UK) using standard electroblotting protocols. Membranes were subjected to blocking procedures using appropriate blocking buffer for 1 hour at ambient temperature, followed by overnight incubation at 4°C with primary antibodies directed against target proteins. Primary antibody specifications and dilutions are detailed in the accompanying antibody table. After primary antibody incubation, membranes were subjected to stringent washing protocols and incubated with horseradish peroxidase-conjugated secondary antibodies for 1 hour at room temperature. Protein detection was achieved using enhanced chemiluminescence substrate (Pierce ECL, Thermo Fisher Scientific) and band quantification was performed using ImageQuant

TL software (version 8.1, Amersham Biosciences) for densitometric analysis.

2.12. Immunofluorescence microscopy analysis

Confocal immunofluorescence analysis was performed to assess spatial distribution and expression patterns of prohibitin in cultured adipocyte populations. Preadipocytes were seeded at 4×10^3 cells per chamber in 8-well chamber slide systems (Thermo Fisher Scientific) and subjected to differentiation protocols as previously described. Following experimental treatments, cells were subjected to permeabilization using 0.1% Triton X-100 detergent solution for 30 minutes, followed by fixation in 4% paraformaldehyde solution for 30 minutes at ambient temperature. Permeabilized and fixed cells were subjected to blocking procedures using 1% bovine serum albumin in Tween 20-supplemented phosphate-buffered saline for 1 hour to prevent non-specific antibody binding. Primary antibody incubation was performed overnight at 4°C using prohibitin-specific antibodies at optimized dilutions. Following primary antibody incubation, cells were subjected to stringent washing protocols using phosphate-buffered saline and incubated with fluorescent secondary antibodies. Nuclear visualization was achieved using DAPI mounting medium (Sigma-Aldrich, Merck KGaA, Darmstadt, Germany) with 30-second incubation at 37°C under light-protected conditions. Fluorescence imaging was performed using confocal laser scanning microscopy (LSM 800, Carl Zeiss, Jena, Germany) with appropriate excitation and emission wavelengths for multi-channel fluorescence detection. Image acquisition parameters were standardized across all experimental conditions to enable quantitative fluorescence intensity comparisons.

2.13. Statistical analysis

Results are shown as the mean ± standard error of the mean of triplicate measurements. Normality of the data was assessed with the Shapiro–Wilk test. Comparisons among three or more groups were performed by one-way analysis of variance (ANOVA) followed by Tukey's post hoc multiple comparison test. Statistical analyses were performed with GraphPad Prism 8.3.0 (GraphPad Software, San Diego, USA). Statistical significance was defined as $p < 0.05$, with additional significance levels indicated where appropriate (*$p < 0.05$, **$p < 0.01$).

3. Results

3.1. Synthesis and structural characterization of M13 4E-AHP

The N-terminus of phage coat proteins represents a flexible hydrophilic domain positioned on the external surface of M13 phages, providing an ideal scaffold for peptide insertions (de Medeiros Dantas et al., 2025). To achieve dual functionality for obesity targeting and therapeutic efficacy, we engineered M13 phage using a strategic dual-modification approach targeting both major and minor coat proteins. As illustrated in Fig. 1A, our design incorporated the 4E peptide into the N-terminus of the major coat protein pVIII, enabling high-density presentation of approximately 2,700 copies per phage particle. Simultaneously, the AHP was genetically fused to the minor coat protein pIII, displaying 5 copies at the tail region of the phage. This engineering strategy was specifically designed to optimize both targeting specificity and therapeutic payload density. The pVIII-4E modification provides abundant biochemical signaling capability across the entire phage nanofiber surface, while the pIII-AHP insertion enables selective recognition and binding to prohibitin receptors highly expressed in white adipose tissue endothelial cells. Structural integrity and morphological

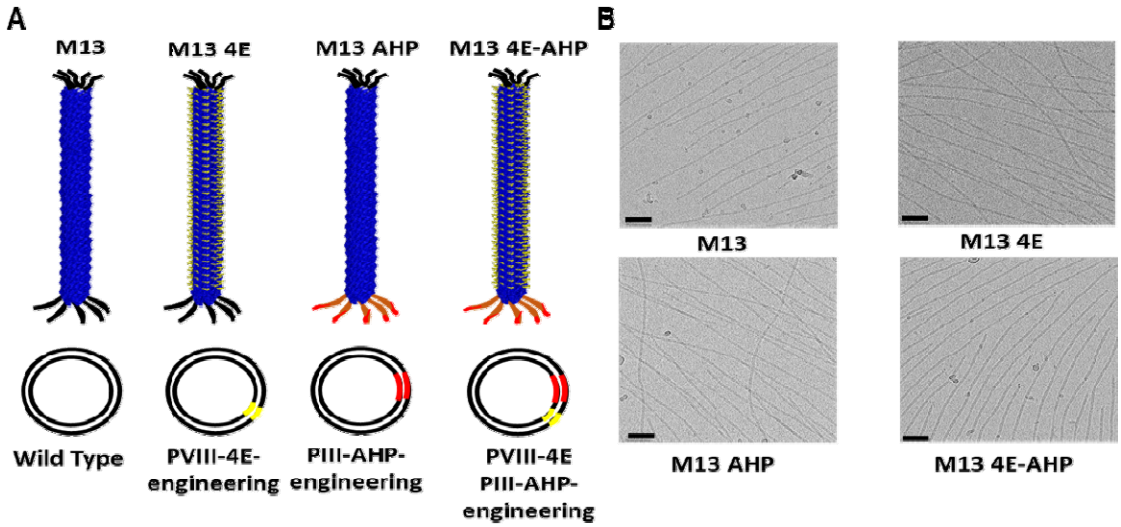


Fig. 1. Engineering and characterization of M13 4E-AHP M13 phage. (A) Schematic representation of M13 phage variants showing wild-type M13, M13 4E (pVIII-4E engineering), M13 AHP (pIII-AHP engineering), and M13 4E-AHP (dual modification). Yellow indicates 4E peptide insertion; red indicates AHP peptide insertion. (B) Cryo-TEM images of M13 phage variants using Krios G4 system. All variants maintain filamentous morphology with preserved structural integrity. Scale bars = 50 nm.

characteristics of the engineered M13 phage variants were examined using Cryo-TEM with a Krios G4 system. High-resolution imaging revealed that all phage variants maintained the characteristic filamentous morphology of wild-type M13 phage (Fig. 1B). Individual phage nanofibers displayed uniform rod-like structures with lengths of approximately 880-900 nm and diameters of 6-7 nm, consistent with previously reported M13 dimensions. Detailed morphological analysis demonstrated that neither the 4E modification in pVIII nor the AHP insertion in pIII significantly altered the overall structural architecture of the M13 phage particles. All engineered variants (M13 4E, M13 AHP, and M13 4E-AHP) preserved the native helical assembly and filamentous organization characteristic of wild-type M13. The phage particles exhibited consistent diameter uniformity along their length and maintained typical flexibility patterns observed in native M13 structures. Importantly, no evidence of structural aberrations, aggregation, or morphological distortions was observed in any of the engineered variants, indicating that the dual modification strategy successfully preserved phage structural integrity while introducing the desired functional peptides.

To further evaluate the physicochemical characteristics of the engineered M13 phage variants, DLS analysis was conducted to assess hydrodynamic size, surface charge, and colloidal stability (Table 2). The hydrodynamic size profiles showed clear differences among the variants. Wild-type M13 presented an average diameter in the lower 80-nanometer range, consistent with the expected dimensions of filamentous phage particles in aqueous solution. The M13 4E variant displayed a noticeably larger size, with values exceeding wild-type by nearly one-third, suggesting that incorporation of the 4E motif induced conformational adjustments or enhanced hydration around the viral filament. The

Table 2. Physicochemical characterization of M13 phage variants by dynamic light scattering

Parameters	M13	M13 4E	M13 AHP	M13 4E-AHP
Z-average (nm)	82.36 ± 2.54	111.36 ± 3.12	83.43 ± 4.54	113.36 ± 4.39
Zeta potential (mV)	-43.5 ± 0.9	-51.6 ± 1.2	-41.2 ± 1.6	-50.9 ± 1.7
PDI	0.357 ± 0.045	0.289 ± 0.014	0.336 ± 0.036	0.296 ± 0.057
Conductivity (mS/cm)	0.0238 ± 0.0034	0.0495 ± 0.0025	0.0229 ± 0.0036	0.0487 ± 0.0049

Values represent mean ± standard deviation (n=3).
Z-average indicates hydrodynamic diameter; PDI, polydispersity index.

M13 AHP variant exhibited a size comparable to wild-type, indicating that insertion of AHP had little impact on overall hydrodynamic behavior. The dual-modified M13 4E-AHP showed a diameter similar to that of the 4E-only variant, reflecting the combined influence of both peptide modifications. Zeta potential measurements further highlighted the electrostatic consequences of peptide incorporation. Wild-type M13 carried a strongly negative surface charge of approximately −44 mV. The 4E modification further increased this negativity by close to 20%, attributable to the additional acidic residues present on the phage surface. By contrast, the AHP variant slightly reduced the net negative charge, consistent with the contribution of basic residues within the AHP sequence that partially counterbalanced the intrinsic surface potential. The dual-modified phage restored a highly negative charge, comparable to that of the 4E-only variant, indicating that the acidic contribution from the 4E motif predominated over the compensatory positive charges in AHP. PDI values provided further insights into sample uniformity. Wild-type phage showed moderate heterogeneity typical of biological nanostructures. Introduction of the 4E sequence resulted in a more uniform population, with PDI values reduced by roughly 20% relative to wild-type. The AHP-modified phage maintained a distribution similar to wild-type, while the dual-modified phage exhibited PDI values closer to the more uniform 4E profile, confirming that all variants remained within acceptable stability ranges. Conductivity measurements revealed additional differences aligned with peptide composition. Wild-type phage displayed a baseline conductivity in the range of 0.02 mS/cm. The 4E modification approximately doubled this value, reflecting the substantial ionic contribution from multiple glutamic acid residues. The AHP variant, in contrast, exhibited conductivity almost identical to wild-type, suggesting that its mixed amino acid sequence contributed little to ionic strength. The dual-modified 4E-AHP phage again showed conductivity values nearly two-fold greater than wild-type, paralleling the effect of the 4E modification alone and underscoring the dominant role of the glutamate-rich motif. Taken together, these DLS characterizations confirm that the engineered M13 phage variants preserved favorable colloidal stability and structural integrity, while exhibiting distinct and predictable physicochemical alterations arising from their specific peptide modifications.

3.2. Validation of prohibitin engagement by M13 AHP in differentiated adipocytes

To validate the functional activity of the M13 AHP, prohibitin-associated signals were examined in both preadipocytes and differentiated adipocytes. Prohibitin, a well-established vascular receptor highly enriched in white adipose tissue, represents the primary binding partner for AHP peptides. Immunofluorescence microscopy demonstrated distinct prohibitin

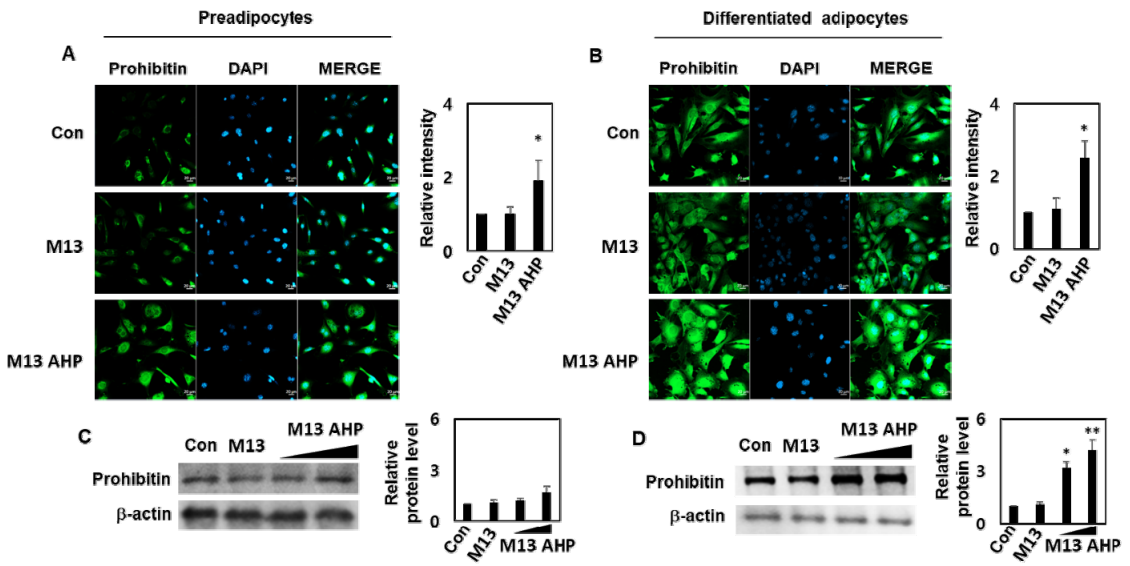


Fig. 2. Functional validation of AHP targeting through prohibitin expression analysis in preadipocytes and differentiated adipocytes. (A-B) Immunofluorescence microscopy analysis of prohibitin expression (green) with DAPI nuclear counterstaining (blue) in (A) preadipocytes and (B) differentiated adipocytes treated with control medium, wild-type M13, or M13 AHP for 24 hours. Right panels show quantitative analysis of relative fluorescence intensity. Scale bars = 25 μm. (C-D) Western blot analysis of prohibitin protein expression with β-actin loading controls in (C) preadipocytes and (D) differentiated adipocytes. Right panels show densitometric quantification of relative protein levels normalized to β-actin. Data represent mean ± SEM from three independent experiments. Statistical significance: *p < 0.05 vs. control group.

staining patterns depending on cell state and treatment (Fig. 2A-B). In untreated preadipocytes, prohibitin signals were faint and appeared as sparse puncta scattered across the cells. Differentiated adipocytes, by contrast, displayed markedly stronger prohibitin-associated fluorescence, consistent with their vascular-like phenotypic features acquired during adipogenic maturation. Quantitative assessment supported these observations: in preadipocytes, prohibitin fluorescence intensity remained low across treatments, with relative values near baseline for controls, a slight elevation with wild-type M13, and a modest rise with M13 AHP treatment. Even with this increase, signal levels in preadipocytes were still less than half of those recorded in differentiated adipocytes. In differentiated adipocytes, M13 exposure produced little to no alteration compared to controls, whereas M13 AHP treatment yielded a pronounced intensification of prohibitin-associated fluorescence, approximately doubling the values observed in untreated cells. Confocal imaging further revealed more concentrated and spatially organized fluorescence patterns following M13 AHP exposure, indicative of stable receptor–ligand engagement rather than new prohibitin synthesis. Western blotting corroborated the microscopy data (Fig. 2C-D). Prohibitin protein was consistently low in preadipocytes across all conditions, with densitometric measurements showing only slight variation. In differentiated adipocytes, prohibitin levels were substantially higher overall, reflecting differentiation-dependent upregulation. Importantly, M13 AHP treatment produced a striking increase in

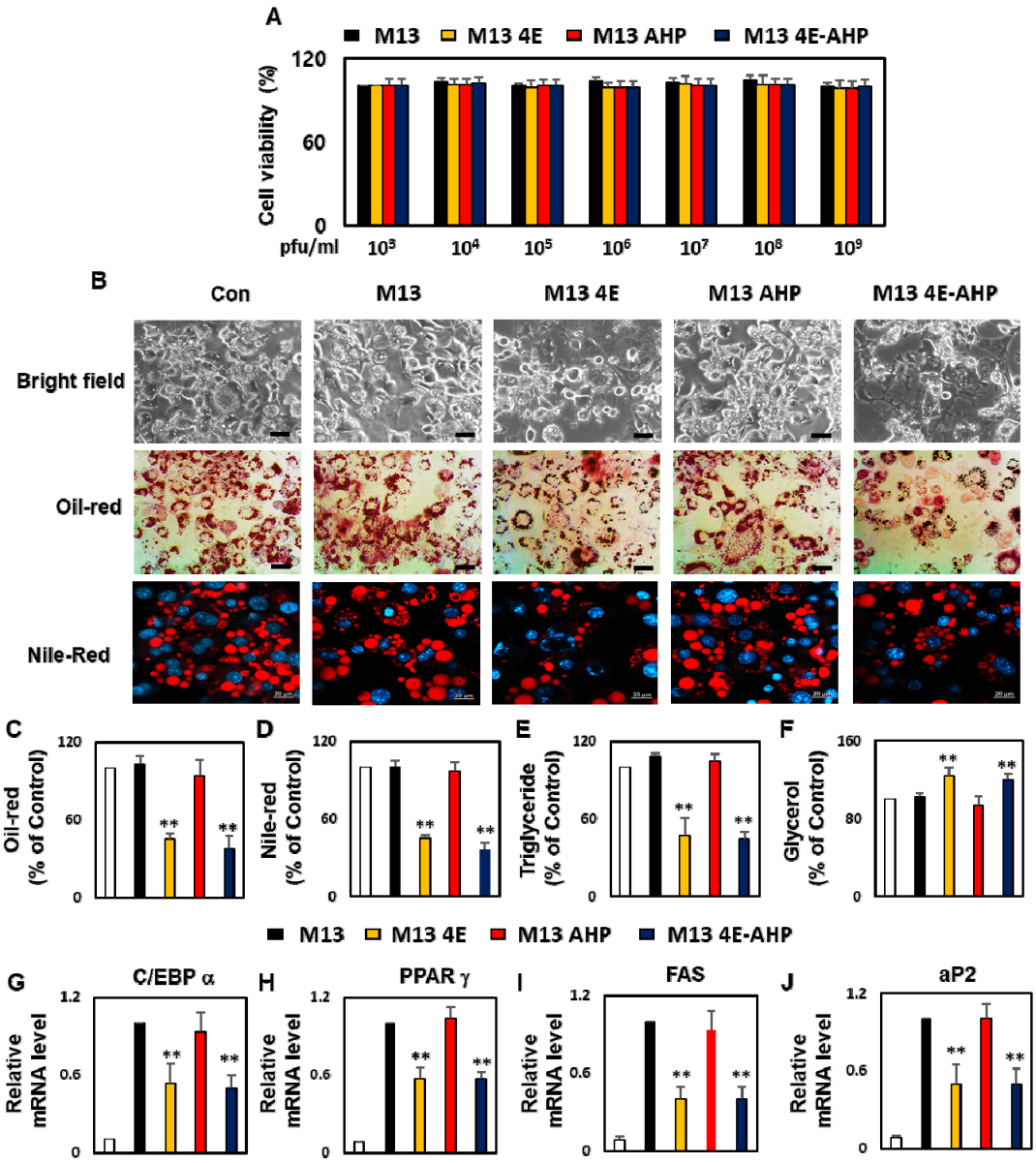


Fig. 3. Anti-adipogenic effects of M13 phage variants on preadipocyte differentiation and lipid accumulation. (A) Cell viability assessment by CCK-8 assay across logarithmic phage concentrations (10^3–10^9 PFU/mL) demonstrating excellent biocompatibility (>97% viability) for all variants. (B) Representative microscopic analysis of adipocyte differentiation: bright-field morphology (top), Oil Red-O staining for neutral lipids (middle), and Nile Red fluorescence with DAPI nuclear counterstaining (bottom). Scale bars = 50 μm for bright-field and Oil Red-O; 25 μm for Nile Red images. (C–F) Quantitative biochemical analysis: (C) Oil Red-O extraction and spectrophotometric quantification, (D) Nile Red fluorescence intensity assessment, (E) Direct intracellular triglyceride measurement, (F) Glycerol quantification for metabolic activity assessment. (G–J) Molecular analysis of adipogenic gene expression by quantitative RT-PCR: (G) C/EBPα, (H) PPARγ, (I) FAS, (J) aP2. **$p < 0.01$ vs. control group. Con, control (MDI-induced differentiation without phage treatment).

prohibitin band intensity relative to both controls and wild-type M13. Quantitative analysis indicated that prohibitin protein levels in M13 AHP–treated differentiated adipocytes were nearly three times greater than baseline, clearly exceeding the modest changes observed under other conditions. Taken together, these findings demonstrate that the AHP moiety displayed on M13 phage retains its functional binding capacity, selectively engaging prohibitin receptors in differentiated adipocytes and thereby validating the intended engineering strategy.

3.3. Comprehensive anti-adipogenic analysis of M13 4E-AHP on preadipocyte differentiation and metabolic reprogramming

Cell viability assessed using the CCK-8 assay confirmed excellent biocompatibility of all engineered M13 variants over a wide therapeutic concentration range (Fig. 3A). The assay, which quantifies metabolically active cells through mitochondrial dehydrogenase activity, showed that across seven concentration points spanning six orders of magnitude, all phage groups—including wild-type M13, M13 4E, M13 AHP, and M13 4E-AHP—maintained cell viability close to baseline levels, with only minor variation among treatments. Importantly, no concentration-dependent cytotoxicity was observed, supporting the interpretation that anti-adipogenic effects resulted from specific pathway modulation rather than nonspecific stress. To define a safe working range, cells were exposed to each phage variant at seven concentrations (10^3–10^9 PFU/mL) for 24 h, and viability was determined by the CCK-8 assay. As no cytotoxicity was detected over the entire range (viability >97%), 1×10^7 PFU/mL was selected as the working concentration for all differentiation experiments. The same concentration was used for all variants to allow direct comparison. Endotoxin content at this concentration was low and comparable among preparations. Bright-field microscopy provided additional morphological insight (Fig. 3B, top panel). Control preadipocytes exposed to the MDI differentiation cocktail underwent the expected transition from elongated fibroblast-like cells to large, rounded adipocytes filled with prominent lipid vacuoles over the 9-day period. Cells treated with wild-type M13 or M13 AHP followed a similar trajectory, forming abundant spherical adipocytes indistinguishable from controls, indicating that neither the unmodified phage nor AHP insertion alone interfered with differentiation. In contrast, M13 4E treatment markedly preserved the elongated preadipocyte phenotype, with cells showing reduced cytoplasmic enlargement. The dual-modified 4E-AHP variant produced a comparable effect, with cells maintaining spindle-like morphology and minimal vacuole accumulation, suggesting strong inhibition of the adipogenic transcriptional program. Oil Red-O staining, the standard method for visualizing neutral lipid deposition, confirmed these observations (Fig. 3B, middle panel). Control cultures developed dense and uniform red staining consistent with robust triglyceride accumulation, and both wild-type M13 and M13 AHP produced similar patterns. In comparison, the 4E-containing variants showed markedly reduced staining, with signal intensities dropping to less than half of control levels. The dual-modified phage was equally effective as the 4E variant alone, with both showing only sparse staining across the population. Quantitative spectrophotometric analysis paralleled these results (Fig. 3C), with lipid content remaining near or slightly below control values for wild-type M13 and AHP, but decreasing by roughly 40–60% in the 4E and 4E-AHP groups. Nile Red staining provided complementary evaluation of intracellular lipid droplets (Fig. 3B, bottom panel). Control adipocytes displayed

abundant large lipid inclusions with intense red fluorescence. Wild-type M13 and AHP-treated cultures showed little change, maintaining fluorescence intensities close to controls. By contrast, both 4E and 4E-AHP treatments drastically reduced the number and size of lipid droplets, resulting in much weaker fluorescence signals. Quantitative analysis confirmed that lipid fluorescence in 4E-containing groups was reduced by over half relative to controls (Fig, 3D). Direct enzymatic measurement of intracellular triglycerides corroborated these findings (Fig. 3E). Control adipocytes exhibited a near doubling of triglyceride content compared to undifferentiated precursors, consistent with successful metabolic reprogramming. Wild-type M13 and AHP produced only slight changes, remaining essentially comparable to controls. In sharp contrast, the 4E and 4E-AHP groups showed triglyceride levels cut to less than half of control values, indicating robust inhibition of lipid storage capacity. Glycerol assays further supported these metabolic effects (Fig. 3F). While control adipocytes maintained baseline glycerol consistent with active triglyceride synthesis, both 4E and 4E-AHP treatments increased glycerol release above control levels by about 10-20%, suggesting either enhanced lipolysis or reduced incorporation of glycerol into triglycerides. Molecular analysis by quantitative RT-PCR demonstrated that these morphological and metabolic effects were driven by suppression of key transcriptional regulators (Fig. 3G–J). C/EBPα expression, essential for late-stage differentiation, was reduced by roughly half in the 4E and 4E-AHP groups. PPARγ, the master regulator of adipogenesis, showed a similar decrease, with expression dropping to nearly one-half of control levels. Fatty acid synthase (FAS), the rate-limiting enzyme in lipid biosynthesis, was also markedly downregulated, falling to about one-third of control expression in dual-modified phage–treated cells. Adipocyte protein 2 (aP2) followed the same trend, declining to well below half of baseline levels. In contrast, wild-type M13 and AHP-treated cultures maintained expression levels close to those of untreated controls, generally within ±10% variation. Together, these results demonstrate that incorporation of the 4E motif—alone or in combination with AHP—selectively suppresses adipogenic differentiation by interfering with lipid accumulation, triglyceride synthesis, and transcriptional regulation, while maintaining cell viability. These findings confirm that the engineered 4E-AHP phage exerts its anti-adipogenic effects through targeted modulation of the adipogenic program rather than nonspecific cytotoxicity.

4. Discussion

The development of obesity as a global epidemic necessitates innovative therapeutic strategies that address the fundamental biological mechanisms underlying adipose tissue dysfunction (Yang et al., 2023). This study presents the first demonstration of genetically engineered M13 phage as a dual-functional biological macromolecule platform for targeted obesity intervention, combining tissue-specific delivery with direct anti-adipogenic therapeutic activity. The comprehensive characterization data confirms that genetic modification of M13 phage to incorporate both AHP and 4E peptide sequences maintains the essential structural and functional properties of the native viral scaffold. Cryo-TEM analysis revealed preservation of the characteristic filamentous morphology. The observed physicochemical changes in surface charge and hydrodynamic properties, rather than representing structural compromises, actually enhance the therapeutic characteristics of the

platform by potentially improving cellular interactions and tissue penetration. The successful high-density display of the 4E peptide on the major coat protein pVIII represents a significant achievement in biological macromolecule engineering. With approximately 2,700 copies per phage particle, this configuration provides therapeutic payload density that far exceeds conventional drug delivery systems while maintaining the biocompatibility advantages of biological macromolecules over synthetic alternatives.

The identification of the 4E tetrapeptide as the primary bioactive component represents a paradigm shift in obesity therapeutics. Unlike conventional approaches that target systemic metabolic pathways or behavioral modifications, the 4E peptide operates through direct cellular intervention at the level of adipogenic differentiation. The tetrapeptide's composition of four glutamic acid residues creates a highly negatively charged domain that appears to interfere with fundamental cellular processes governing lipid synthesis and storage. The mechanism of 4E-mediated anti-adipogenic activity likely involves disruption of transcriptional cascades essential for preadipocyte maturation. The preserved preadipocyte morphology observed in 4E-treated cultures, combined with dramatic reductions in lipid accumulation markers across multiple complementary assays, suggests interference with key regulatory pathways such as PPARγ activation or C/EBP transcription factor function (Kim et al., 2023; Lin et al., 2024). This cellular-level intervention provides therapeutic control that is both specific and comprehensive, addressing the fundamental biological processes underlying obesity development (Kagawa et al., 2023).

The functional validation of AHP-mediated targeting through prohibitin receptor engagement demonstrates the successful implementation of tissue-specific delivery within the engineered phage platform (Xiao et al., 2024). The selective upregulation of prohibitin expression in differentiated adipocytes following M13 AHP treatment confirms active receptor–ligand interactions and validates the biological relevance of this targeting mechanism. The specificity of AHP targeting addresses a critical limitation of current obesity therapeutics—the inability to concentrate therapeutic activity at sites of pathological fat accumulation. By enabling preferential delivery to adipose tissue, the AHP component allows for dose optimization strategies that maximize therapeutic efficacy while minimizing systemic exposure and potential adverse effects (Salameh et al., 2016; Daquinag et al., 2021; Safari et al., 2022). The increase in prohibitin-associated signals after M13 AHP treatment, which was not observed with wild-type M13, is consistent with AHP-dependent engagement of prohibitin. However, this observation alone is insufficient to establish selective targeting, for several reasons. First, we measured prohibitin signal intensity and protein level, not phage binding or internalization; therefore, whether the signal change reflects direct ligand–receptor binding, altered receptor clustering or stability, or changes in epitope accessibility cannot be distinguished. Second, a modest increase was also observed in preadipocytes, indicating that the selectivity for differentiated adipocytes is relative rather than absolute. Third, we did not include a non-targeting control phage displaying a scrambled peptide, which would more rigorously demonstrate sequence specificity. Fourth, prohibitin–AHP targeting was originally described on the vasculature of white adipose tissue, whereas the 3T3-L1 monoculture used here lacks vascular endothelium and therefore does not recapitulate this targeting context. Further studies, including competition assays

with free AHP peptide, prohibitin knockdown, co-localization of phage particles with prohibitin, and in vivo biodistribution analysis, are needed to establish the targeting function of AHP. The integration of AHP targeting with 4E therapeutic activity within a single macromolecular platform represents a sophisticated approach to precision medicine that simultaneously addresses both the spatial and temporal aspects of therapeutic intervention.

The comprehensive in vitro characterization of the M13 4E-AHP platform provides compelling evidence for its therapeutic potential at the cellular level. The observed effects across multiple endpoints—preserved preadipocyte morphology, reduced lipid accumulation, modulated glycerol metabolism, and suppressed expression of master adipogenic transcription factors—establish this biological macromolecule system as a mechanistically robust therapeutic candidate. The convergent evidence from morphological, biochemical, and molecular analyses indicates that 4E-mediated intervention operates through coordinated disruption of the adipogenic transcriptional program rather than through nonspecific cytotoxic effects, as confirmed by the preservation of cell viability across all tested concentrations. This mechanistic specificity suggests that 4E-mediated intervention may modulate fundamental adipogenic pathways with therapeutic relevance extending beyond simple lipid accumulation, warranting further investigation into its broader effects on cellular metabolism and differentiation programs. M13 4E and M13 4E-AHP showed comparable suppression of adipogenic differentiation and lipid accumulation, whereas M13 AHP alone had no appreciable effect. This indicates that the anti-adipogenic activity arises from the 4E peptide displayed on pVIII, and that AHP does not itself contribute to this activity. The similarity is not unexpected in our experimental setting: in a monolayer culture the phage is added directly to the medium, so all cells are exposed regardless of any targeting ligand, and the advantage of a homing peptide—enrichment at the target tissue—cannot manifest. The significance of adding AHP therefore lies in other aspects. First, dual display on pIII and pVIII did not compromise the structural integrity , colloidal properties, or anti-adipogenic activity of the 4E phage, demonstrating that the two functions can be combined on a single scaffold. Second, M13 4E-AHP retains the prohibitin-associated activity conferred by AHP, which is expected to be relevant for adipose tissue homing in vivo, where biodistribution determines the effective dose reaching adipose tissue. Whether this translates into improved efficacy over M13 4E alone can only be answered by in vivo studies.

While this study provides comprehensive in vitro validation of the M13 4E-AHP platform, several areas warrant further investigation prior to clinical translation. In vivo efficacy and safety studies are essential to establish whether the anti-adipogenic effects observed at the cellular level translate into meaningful physiological outcomes in a living organism, including effects on body weight, adipose tissue mass, and systemic metabolic parameters. Long-term safety studies and dose–response relationships also require detailed characterization to establish optimal therapeutic protocols. The mechanism of 4E peptide action, while functionally validated at the cellular and molecular level, would benefit from detailed molecular pathway analysis to enable rational optimization of therapeutic activity. Future research directions should explore in vivo validation in animal models of obesity, the potential for combination therapies, dose optimization strategies, and application to related metabolic disorders. The modular nature of the phage platform enables incorporation of additional therapeutic peptides or targeting

moieties for enhanced efficacy or expanded therapeutic applications. This study has several limitations. First, all experiments were performed in the murine 3T3-L1 cell line, which does not reflect the complexity of adipose tissue in vivo, including vascular endothelium, immune cells, and systemic metabolic regulation; confirmation in primary or human adipocytes is also desirable. Second, phage treatment was applied before and during differentiation, so the results demonstrate inhibition of adipogenesis rather than reversal of lipid accumulation in established mature adipocytes. Third, only a single working concentration was evaluated for differentiation endpoints, and dose–response relationships were not characterized. Fourth, mechanistic insight is limited to mRNA expression of adipogenic markers (C/EBPα, PPARγ, FAS, aP2); protein-level and upstream pathway analyses, as well as the mechanism by which the 4E peptide acts on cells, remain to be clarified. Fifth, phage-specific issues relevant to therapeutic use, such as biodistribution, clearance, immunogenicity, and long-term safety, cannot be assessed in vitro. Therefore, the present findings should be regarded as proof-of-concept at the cellular level and do not by themselves establish applicability to obesity treatment. Future studies in diet-induced obese mouse models are required to evaluate whether M13 4E-AHP reduces body weight and adipose tissue mass, to determine biodistribution and the contribution of AHP to adipose targeting (by comparison with M13 4E), and to assess safety and immunogenicity.

5. Conclusions

This investigation establishes M13 4E-AHP phage as a novel biological macromolecule platform for obesity treatment through dual-functional integration of targeted delivery and anti-adipogenic activity. The engineered system maintains structural integrity while displaying the 4E tetrapeptide as the primary bioactive component and AHP for tissue-specific targeting via prohibitin receptor engagement. In vitro studies demonstrated substantial lipid accumulation reduction and suppression of master adipogenic transcription factors in 3T3-L1 adipocytes, with excellent biocompatibility maintained across all tested concentrations. The biological macromolecule approach offers superior biocompatibility and biodegradability compared to synthetic delivery systems, with high-density therapeutic peptide presentation that exceeds conventional platforms. This research validates phage-based therapeutics as viable candidates for precision medicine applications and establishes a strong foundation for targeted metabolic interventions, warranting further in vivo investigation to confirm clinical translation potential.

Acknowledgments

This Work was supported by a 2-Year Research Grant of Pusan National University.

REFERENCES

Antwi, F., Fazylova, N., Garcon, M., Lopez, L., Rubiano, R., Slyer, J. T., 2012, The effectiveness of web-based programs on the reduction of childhood obesity in school-aged children: A Systematic review, JBI Libr. Syst. Rev., 10, 1-14.

Ataey, A., Jafarvand, E., Adham, D., Moradi-Asl, E., 2020, The relationship between obesity, overweight, and the Human Development Index in World Health Organization Eastern Mediterranean Region countries, J. Prev. Med. Public Health, 53, 98-105.

Chang, C., Guo, W., Yu, X., Guo, C., Zhou, N., Guo, X., Huang, R., Li Q., Zhu Y., 2023, Engineered M13 phage as a novel therapeutic bionanomaterial for clinical applications: From tissue regeneration to cancer therapy, Mater. Today Bio, 20, 100612.

Daquinag, A. C., Gao, Z., Fussell, C., Immaraj, L., Pasqualini, R., Arap, W., Akimzhanov, A., Febbraio, M., Kolonin M., 2021, Fatty acid mobilization from adipose tissue is mediated by CD36 posttranslational modifications and intracellular trafficking, JCI Insight, 6, e147057.

de Medeiros Dantas, J. M., Kabir, R. F., Modafferi, D., Ozbaran, B., Dorval Courchesne, N., 2025, M13 bacteriophage as a versatile platform for the creation of new materials via genetic engineering, Can. J. Microbiol., 71, 1-18.

Fadaie, M., Dianat-Moghadam, H., Ghafouri, E., Naderi, S., Darvishali, M. H., Ghovvati, M., Khanahmad, H., Boshtam M., Makvandi, P., 2023, Unraveling the potential of M13 phages in biomedicine: Advancing drug nanodelivery and gene therapy, Environ. Res., 238, 117132.

Gao, M., Zhao, Z., Lv, P., Li, Y., Gao, J., Zhang, M., Zhao, B., 2015, Quantitative combination of natural anti-oxidants prevents metabolic syndrome by reducing oxidative stress, Redox Biol., 6, 206-217.

Gao, Z., Daquinag, A. C., Fussell, C., Djehal, A., Désaubry, L., Kolonin, M. G., 2021, Prohibitin inactivation in adipocytes results in reduced lipid metabolism and adaptive thermogenesis impairment, Diabetes, 70, 2204-2212.

Gu, Y., Iannuzzelli, J. A., Fasan, R., 2022, MOrPH-PhD: A Phage display system for the functional selection of genetically encoded macrocyclic peptides, Methods Mol. Biol., 2371, 261-286.

Jin, H., Lee, S., 2018, Engineering of M13 bacteriophage for development of tissue engineering materials, Methods Mol. Biol., 1776, 487-502.

Jin, X., Qiu, T., Li, L., Yu, R., Chen, X., Li, C., Proud, C., Jiang, T., 2023, Pathophysiology of obesity and its associated diseases, Acta Pharm. Sin. B, 13, 2403-2424.

Kagawa, S., Tanabe, K., Hiromura, M., Ogawa, K., Koga, T., Maeda, T., Amo-Shiinoki, K., Ochi, H., Ichiki, Y., Fukuyama, S., Suzuki, N., Ohmine, T., Hamachi, S., Tsuneki, H., Okuya, S., Sasaoka, T,. Tanizawa, Y., Nagashima, F., 2023, Hachimijiogan, a traditional herbal medicine, modulates adipose cell function and ameliorates diet-induced obesity and insulin resistance in mice, Front. Pharmacol., 14, 1167934.

Kim, M. S., Baek, J., Lee, J., Sivaraman, A., Lee, K., Chun, K., 2023, Deubiquitinase USP1 enhances CCAAT/enhancer-binding protein beta (C/EBPβ) stability and accelerates adipogenesis and lipid accumulation, Cell Death Dis., 14, 776-777.

Kim, S., Heo, H. R., Kim, C. S., Shin, H. H., 2024, Genetically engineered bacteriophages as novel nanomaterials: Applications beyond antimicrobial agents, Front. Bioeng. Biotechnol., 12, 1319830.

Kong, Y., Yang, H., Nie, R., Zhang, X., Zuo, F., Zhang, H., Nian, X., 2025, Obesity: Pathophysiology and therapeutic interventions, Mol. Biomed., 6, 25-29.

Li, X., Wang, Z., Jiang, J., Shen, C., 2022, Role of polyphenols from Polygonum multiflorum Caulis in obesity-related disorders, J. Ethnopharmacol., 294, 115378.

Lin, S., Yang, C., Jiang, R., Wu, C., Lang, D., Wang, Y., Li, X, Jiang, C., Liu, Q., Shen, C., 2024, Flavonoid extracts of Citrus aurantium L. var. amara Engl. promote browning of white adipose tissue in high-fat diet-induced mice, J. Ethnopharmacol., 324, 117749.

Mahamat-Saleh, Y., Aune, D., Freisling, H., Hardikar, S., Jaafar, R., Rinaldi, S., Gunter, M., Dossus, L., 2024, Association of metabolic obesity phenotypes with risk of overall and site-specific cancers: A Syst ematic review and meta-analysis of cohort studies, Br. J. Cancer, 131, 1480-1495.

Nazeri, N., Bahrami, Y., Barzegari, E., Mohammadi, M., Kazemi-Lomedasht, F., Rajabibazl, M., Mohammadzadeh, S., 2025, Engineering M13 bacteriophage to display HER2 mimotopes on pVIII for vaccine development, Sci. Rep., 15, 22285.

Pati, S., Irfan, W., Jameel, A., Ahmed, S., Shahid, R. K., 2023, Obesity and cancer: A Current overview of epidemiology, pathogenesis, outcomes, and management, Cancers (Basel), 15, 485, doi: 10.3390/cancers15020485

Rahimi, A., Soudi, S., Vakilian, S., Jamshidi-Adegani, F., Sadeghizadeh, M., Al-Hashmi, S., 2023, Bacteriophage M13 modulates the sepsis-related inflammatory responses and organ damage in a CLP model, Shock, 59, 493-504.

Rupert, J. E., Kolonin, M. G., 2022, Fatty acid translocase: A Culprit of lipid metabolism dysfunction in disease, Immunometabolism (Cobham), 4, e00001.

Safari, Z., Sadeghizadeh, M., Asgaritarghi, G., Bardania, H., Sadeghizadeh, D., Soudi, S., 2022, M13 phage coated surface elicits an anti-inflammatory response in BALB/c and C57BL/6 peritoneal macrophages, Int. Immunopharmacol., 107, 108654.

Salameh, A., Daquinag, A. C., Staquicini, D. I., An, Z., Hajjar, K. A., Pasqualini, R., Arap, W., Kolonin, M., 2016, Prohibitin/annexin 2 interaction regulates fatty acid transport in adipose tissue, JCI Insight, 1, e86351.

Soundharrajan, I., Kuppusamy, P., Srisesharam, S., Lee, J. C., Sivanesan, R., Kim, D., Choi, K., 2020, Positive metabolic effects of selected probiotic bacteria on diet-induced obesity in mice are associated with improvement of dysbiotic gut microbiota, FASEB J., 34, 12289-12307.

Wang, R., Li, H., Cao, Y., Wang, Z., Yang, T., Wang, J., 2023, M13 phage: A Versatile building block for a highly specific analysis platform, Anal. Bioanal. Chem., 415, 3927-3944.

Wang, S., Uchida, N., Ueno, K., Matsubara, T., Sato, T., Aida, T., Ishida, Y., 2023, Effects of the magnetic orientation of M13 bacteriophage on phage display selection, Chemistry-A Eropean J., 29, e202302261.

Xiao, Q., Tang, L., Chen, S., Mei, Y., Wang, C., Yang, J., Shang, J., Li, S., Wang, W., 2024, Two-pronged attack: Dual activation of fat reduction using near-infrared-responsive nanosandwich for targeted anti-obesity treatment, Adv. Sci. (Weinh), 11, e2406985.

Xian, J., Zhong, X., Huang, Q., Gu, H., Feng, Y., Sun, J., Wang, D., Li, J., Zhang, C., Wu, Y., Zhang, J., 2023, N-Trimethylated chitosan coating white adipose tissue vascular-targeting oral nano-system for the enhanced anti-obesity effects of celastrol, Int. J. Biol. Macromol., 236, 124023.

Yang, X., Liang, M., Tang, Y., Ma, D., Li, M., Yuan, C., Hou, y., Sun, C., Liu, J., Wei, Q., Chang, Y., Wang, C., Zhang, J., 2023, KLF7 promotes adipocyte inflammation and glucose metabolism disorder by activating the PKCζ/NF-κB pathway, FASEB J., 37, e23033.

Yang, Y., Chen, I. A., 2024, Visualization of engineered M13 phages bound to bacterial targets by transmission electron microscopy, Methods Mol. Biol., 2793, 175-183.

• Research Professor. Sun Young Park
Institute of Nanobio Convergence, Pusan National University
sundeng99@pusan.ac.kr
• Professor. Jin-Woo Oh
School of Advanced Convergence Future Energy Major, Pusan National University
ojw@pusan.ac.kr
• Professor. Geuntae Park
Convergence Department, Graduate School, Pusan National University
gtpark@pusan.ac.kr